Proton-conducting γ-sulfopropyl Acrylate Tethered Halato-Telechelic PVDF Membranes for Vanadium Redox Flow Batteries

Jeet Sharma, Bruno Améduri, Vaibhav Kulshrestha

ChemElectroChem

Research Article
doi.org/10.1002/celc.202400539

Chemistry Europe
European Chemical Societies Publishing

www.chemelectrochem.org

Proton-conducting γ-sulfopropyl Acrylate Tethered Halato-Telechelic PVDF Membranes for Vanadium Redox Flow Batteries

Jeet Sharma,[a, b, c] Bruno Améduri,*[b] and Vaibhav Kulshrestha*[a, c]

Advanced fluorinated proton-conducting membrane are dominating functional macromolecules due to their high performance in electrochemical energy devices. However, the co-ion leakage and low power densities still proposes a challenge. Herein, a novel functionally tailored polyvinylidene fluoride-*co*-(γ)-sulfopropyl acrylate (PVDF-*g*-SA) based proton-conducting membrane is prepared for vanadium redox flow batteries (VRFBs). The approach introduces a facile guideline to design halato-telechelic $-SO_3H$ architectures by tethering γ-sulfopropyl acrylate onto dehydrofluorinated PVDF. The optimized PVDF-*g*-SA-15 exhibits proton conductivity (κ_m^{H+}) of 17 mS cm^{-1} (*akin* Nafion: ~19 mS cm^{-1}) and retained 87% and >95% of its properties in Fenton's reagent and 3 M H_2SO_4, respectively. In VRFB device, the PVDF-*g*-SA-15 shows ~98% capacity utilization outperforming Nafion-117 (~85%). Moreover, bearing dense ionic orientation (*viz* AFM phases), the potential drop rate is ~2× lower for PVDF-*g*-SA-15 (1.4×10^{-3} V min^{-1}) than that of Nafion-117 (2.6×10^{-3} V min^{-1}). Operational endurance is evaluated fit for 150 mA cm^{-2} showing maximum coulombic, energy and voltage efficiencies of >98%, ~78%, ~80%, respectively. Further investigation for ~200 cycles infer excellent durability with ~95% property retention. Additionally, the PVDF-*g*-SA-15 can deliver ~20% higher power density than Nafion-117 does. Thus, the revealed alternate membrane holds promising utility in VRFB applications.

1. Introduction

Sustainable technologies aimed at achieving net zero-carbon footprints have spurred the development of long-run electrochemical energy storage (EES) devices and the net zero emissions are targeted for 2050, with a goal of reducing emissions by 45% by 2035.[1] Recent developments in material design have facilitated the commercialization of EES grids.[2] Currently, rechargeable vanadium redox flow batteries (VRFBs) are the key technology with the potential to penetrate market installations compared to other RFBs.[2d,e,3] It is anticipated that the future of global energy will significantly rely on VRFB's due to their long-run operational merits where the renewable energy systems destabilize at >20% of energy-generation capacity in decoupled e-storage grids.[1b,4] In VRFB, the proton exchange membrane (PEM) plays a pivotal role in connecting half-cell and facilitates ion transport (*viz* the proton: $H^+(H_2O)_n$) over the bulky redox active bi- (V^{2+}), tri- (V^{3+}) and multi-valent (VO^{2+} and VO_2^+) vanadium ions in the energy storage device.[1a,b,4a] The stability and battery performance of PEMs is governed by its resistance to radicals and electrochemical properties.[5] Presently, Nafion and other derivatives like Aquivion, 3 M membranes are well-known fluorinated polymers (FPs) based PEMs which exhibit high ionic conductivity and possess excellent chemical and oxidative stabilities. The long-side chain architecture (often called halato-telechelic by IUPAC) with highly ionizable sulfonate group and strong C–F bonds in the polymer backbone offers such feature.[6] However, the non-selective ion migration through large percolating pores reduces the capacity and compromises device lifespan.[7] To some extent, the performance of Nafion can be improved through various treatment methods and optimizing thickness. Yet, its high cost limits its widespread terrestrial implementation.[8] Various studies suggest the development of equally efficient alternative membrane materials through a simple synthetic approach.[9] Sulfonated poly(ether ether ketone) is one candidate which shows better electrochemical properties and offer avenues for easy processibility.[10] Unfortunately, the susceptible aryl-oxy bonds undergo oxidative deterioration with each charging cycle (due to VO_2^+).[5b,7c] The rapid oxidation of polymer reduces active V^{5+}-ion (i.e., VO_2^+) concentration per cycle and hence, induces faster energy decay. Generally, the oxidative resistance of sulfonated poly(arylene ether)s can be improved through 2D composite and radical scavenging hydro-

[a] J. Sharma, V. Kulshrestha
Council of Scientific and Industrial Research-Central Salt and Marine Chemicals Research Institute (CSIR-CSMCRI), Bhavnagar, Gujarat 364002, India
E-mail: vaibhavk@csmcri.res.in
vaibhavphy@gmail.com

[b] J. Sharma, B. Améduri
CNRS, ENSCM, University of Montpellier, Institute Charles Gerhardt (ICGM), Montpellier 34293, France
E-mail: bruno.ameduri@enscm.fr

[c] J. Sharma, V. Kulshrestha
Academy of Scientific and Innovative Research (AcSIR), Ghaziabad, Uttar Pradesh 201002, India

Supporting information for this article is available on the WWW under https://doi.org/10.1002/celc.202400539

philic metal oxide intercalation.[11] Nevertheless, the occupancy of composite functional material imparts tortuosity and suppresses the redox active ion crossover and hence preserving the capacity of the battery.[12] Another factor which affects the VRFB performance is hydrodynamic volume transfer. Such a transport behaviour is governed by ionic domain architecture and percolating porosity index of the PEM.[13] Based on previous results, it was worth studying functional modifications applied to the FP backbone with halato-telechelic architectures and, to fabricate a stable and efficient PEM.[9b,14]

Polyvinylidene fluoride (PVDF) stands as a high-grade FP that can be tailored with conducting monomers to engineer stable membranes.[15] In past, Cao et al. designed a highly conducting porous PVDF grafted poly(vinyl pyrrolidone) copolymer membrane in two-step manner via. C–H activation mediated polymerization followed by solvent swelling pretreatment.[16] While, the non-solvent-induced phase inversion was explored by Yoon and coworkers to fabricate membranes with asymmetric pores.[17] Ling et al. reported the VRFB performance of sulfonic silica based porous composite PVDF membranes.[18] Whilst, Yang et al. explored a modification of commercial perfluoro sulfonic acid in PVDF/Nafion blend co-network to overcome the issues of vanadium permeability via sturdy membrane morphology.[19] Similarly, Dalal et al. exploited the Nafion reinforced pore filled PVDF based membrane to reduce active species crossover during charge-discharge operations, PVDF playing a crucial role in overcoming the crossover setbacks.[20] Subsequently, avoiding the Nafion ionomer in matrix, Sreenath et al. fabricated polypropylene supported poly(4-vinyl pyridine) pore-filled proton sponge type separator.[21] Hu et al. designed a challenging dense PEM with highly miscible hydrophilic-hydrophobic sub-nano phase as well as serves dynamic option to acquire high VRFB performance separator.[22] This offers a newer avenue to investigate the solvent processing and monomer compatibility with PVDF. A highly acid resistant poly(VDF-*co*-HFP) grafted sodium styrene sulfonate copolymer membrane was reported by Sharma et al.[23] Later, Rajput et al. designed highly crosslinked poly(VDF-*co*-HFP) based semi-interpenetrated styrene-*co*-divinyl benzene networked membrane.[24] Evidently, these studies suggest strategic designs of stable PEMs from PVDF and its application in VRFBs. Besides composite strategies discussed, it lacks miscible phase morphologies. Moreover, contrasting non-functional monomer grafting onto PVDF which acquires nano-porous architectures restricts PVDF membranes often for flow batteries. Thus, it was of interest to investigate on polybetaine structures with homogenous phase for good proton conductivity and high current density operations ($>100\ mA\,cm^{-2}$).

Herein, a PVDF-*co*-(γ)-sulfopropyl acrylate (PVDF-*g*-SA) copolymer-based PEM is synthesised for VRFB application. The halato-telechelic ionic architecture *akin* Nafion was formulated via simple one-pot post-modification step using highly reactive and proton conducting γ-sulfopropyl acrylate potassium salt monomer and alkali modified dehydrofluorinated PVDF (*d*-PVDF). The strategy aimed at utilizing alkaline susceptibility of PVDF to induce reactive unsaturation sites (i.e., double bonds) for a further grafting of hydrophilic monomer. A plausible mechanism for unprecedented hydrolytic stability of these γ-sulfonated methacrylate-based membrane is suggested. Subsequently, the PVDF-*g*-SA PEMs were evaluated for VRFB, and performances were compared with those of Nafion-117 under similar conditions.

Experimental Section

Materials

The γ-sulfopropyl acrylate potassium salt (γ-SAK) and 2,2′-Azobis-(2-methylpropionitrile) (AIBN) were procured from Sigma Aldrich, USA and AIBN was recrystallized using ethanol for purity. *Fluorinated polymer*: polyvinylidene fluoride (PVDF, Solef® 1015 homopolymer) was supplied by Solvay (now Syensqo) (M_n~230,000; PDI: 2.4 and approx. MFI range of 6–8 g per 10 min at ~230 °C under 2.5 kg load), Nafion-117 was purchased from Sigma Aldrich. *Solvents*: dry Dimethyl acetamide (DMAc), dry Dimethyl formamide (DMF), dry N-Methyl pyrrolidone (NMP) were purchased from S. D Fine-Chem Limited, India. Vanadyl sulphate ($VOSO_4$) was supplied by Sigma Aldrich, USA. Carbon felt of 6 mm thickness was purchased from Nickunj Eximp Entp. Pvt. Ltd. (treated at 400 °C for 4 h). Listed chemicals were used without any further purification step for polyelectrolyte membrane material synthesis. Supporting chemicals (sodium hydroxide, phenolphthalein indicator, ferric chloride, hydrogen peroxide) were purchased from local chemical distributor, Bhavnagar, Gujarat. Milli-pore water (optimum resistivity = 18.2 MΩ cm) was utilized for all the experiments and electrolyte preparation.

Synthesis of poly(vinylidene fluoride)-*co*-(γ)-sulfopropyl acrylate (PVDF-*g*-SA) Membrane

Dehydrofluorination of PVDF

Induction of unsaturation site in PVDF is a crucial step to design PEM. The dehydrofluorination of PVDF was carried out *via* alkali catalysis in solution phase.[25] In brief, to the prepared homogenous solution of PVDF in dimethyl acetamide (~10 w/v%), a predetermined amount (1/10th vol.) of 0.5 M NaOH in iso-propyl alcohol was dropwise added and allowed to react for 12 h. The obtained brown solution was precipitated in distilled water and washed until free from any residual solvent. Finally, the polymer fibres were dried in vacuum oven at 60 °C for 24 h to discard any trapped solvent and labelled as dehydrofluorinated PVDF (*d*-PVDF).[25]

PVDF ^{1}H-NMR (400 MHz in Acetone-d_6): 1.04 ppm ($CH_3CH_2CF_2$–, triplet), 1.81 ppm (–$CH_2CF_2CH_3$, triplet), 2.37 ppm (–$CF_2CH_2CH_2CF_2$–, broad triplet), 2.95 ppm to 2.97 ppm (–$CH_2CF_2CH_2CF_2$–, quintet) and 6.32 ppm (end cap –$CH_2CF_2\underline{H}$, triplet of triplets) (Figure 1a).

***d*-PVDF ^{1}H-NMR (400 MHz in Acetone-d_6)**: 1.04 ppm ($C\underline{H}_3CH_2CF_2$–, triplet), 1.81 ppm (–$\underline{CH}_2CF_2CH_3$, triplet), 2.37 ppm (–$CF_2C\underline{H}_2CH_2CF_2$–, broad triplet), ~2.82 ppm (–$CF_2C\underline{H}_2COC\underline{H}_2CF_2$), 2.95 ppm (solvent water), 2.97 ppm (–$CH_2CF_2C\underline{H}_2CF_2$–, quintet), 5.38 ppm (–(–CH_2–C$\underline{H}$=CF–CH_2–)$_3$–), ~6.0 ppm (–CF_2–C$\underline{H}$=$CFCH_2$–, complex multiplet) and 6.32 ppm (end cap –$CH_2CF_2\underline{H}$, triplet of triplets).

Synthesis of Fluorinated Proton Exchange Membrane

The PVDF-*co*-(γ)-sulfopropyl acrylate PEM was prepared through free radical copolymerization of *d*-PVDF and γ-SAK using recrystallized AIBN as a radical initiator (Scheme 1). In brief, the *d*-PVDF was dissolved in dry N-methyl pyrrolidone at 85 ± 2 °C to yield a

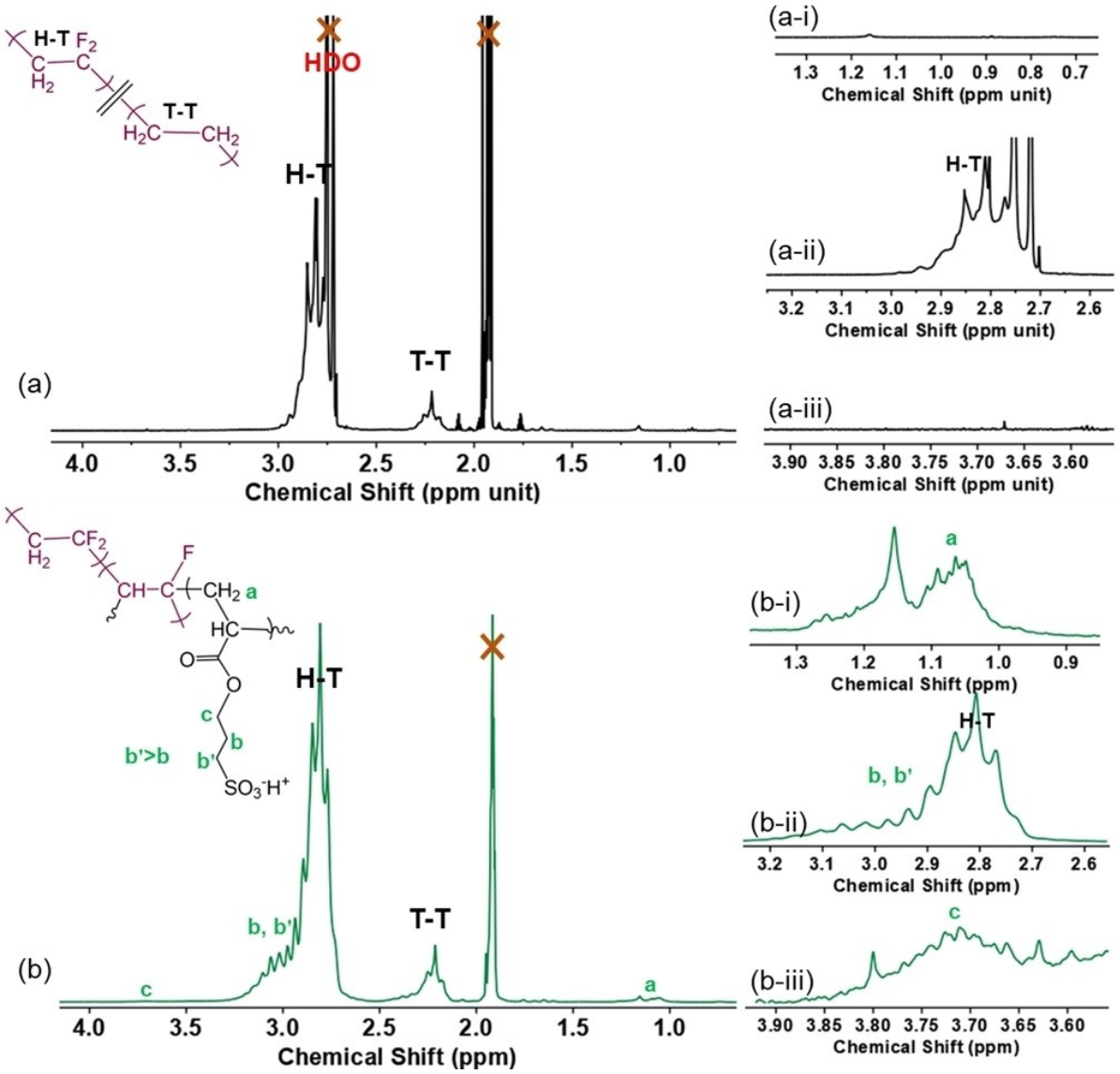

Figure 1. ^{1}H nuclear magnetic resonance spectra recorded in Acetone-d_6; for (a) PVDF, and (b) PVDF-*g*-SA and corresponding deconvoluted spectrum in 0.85–1.37 ppm (region-i), 2.6–3.3 ppm (region-ii) and 3.6–3.9 ppm (region-iii) [on right side].

homogenous solution (*viz* dark brown) and allowed to degas for 10 min. To this degassed *d*-PVDF solution, γ-SAK was added and allowed to dissolve completely under N_2-environment (since, γ-SAK is hygroscopic). Later, AIBN (~10 mg) was added to initiate the copolymerization reaction for the next 12 h and, the functional copolymer was directly casted over a glass plate under the infrared lamp to attain temperature curing phase inversion (RH < 20 %). Finally, the membranes were isolated *via* simple hydrophilicity induced peeling in 0.1 M NaCl to remove any side products. Furthermore, to study the influence of variable monomer concentration on membrane properties and its stabilities, the PVDF-*g*-SA PEM were fabricated with 10, 15 and 20 w/w% γ-SAK concentration with respect to the *d*-PVDF. Finally, the protonated form of copolymer was obtained by immersing the membrane in 0.1 M H_2SO_4 by ion-exchange. Scheme 1 illustrates the synthetic route adopted to fabricate PVDF-*co*-(γ)-sulfopropyl acrylate PEM and Figure S1 illustrates the designed membranes.

PVDF-g-SA ^{1}H-NMR (400 MHz in Acetone-d_6): ~0.8 ppm (–CH_2–$C\underline{H}_2$–CH_2– methylene, quintet), 1.04 ppm ($C\underline{H}_3CH_2CF_2$–, triplet), 1.10 ppm–1.16 ppm (–CF_2–$C\underline{H}_2$–CH–(C=O)–O–CH_2–, broad triplets, homopolymer), 1.81 ppm (–$C\underline{H}_2CF_2CH_3$, triplet), 2.37 ppm (–$CF_2C\underline{H}_2CH_2CF_2$–, broad triplet), ~2.90 ppm (solvent water), 2.97 ppm (–$CH_2CF_2C\underline{H}_2CF_2$–, quintet), 3.1 ppm (–O–CH_2–$C\underline{H}_2$–$C\underline{H}_2$–, complex multiplet), 3.8 ppm (–CH–(C=O)–O–$C\underline{H}_2$–CH_2–), and ~6.2 ppm (end cap –$CH_2CF_2\underline{H}$, triplet of triplets) (Figure 1b).

Physicochemical and Electrochemical Parameter Determination

Physicochemical Analysis

The hydrophilic traits and effect of vanadium electrolyte on designed PVDF-*g*-SA was examined in terms of acid electrolyte uptake (AEU, %), swelling ratio (SR, %), linear expansion ratio (LER, %), ion-exchange capacity (IEC, meq g^{-1}) and vanadium ion uptake (VIU, %), respectively (detailed description in SI-1).

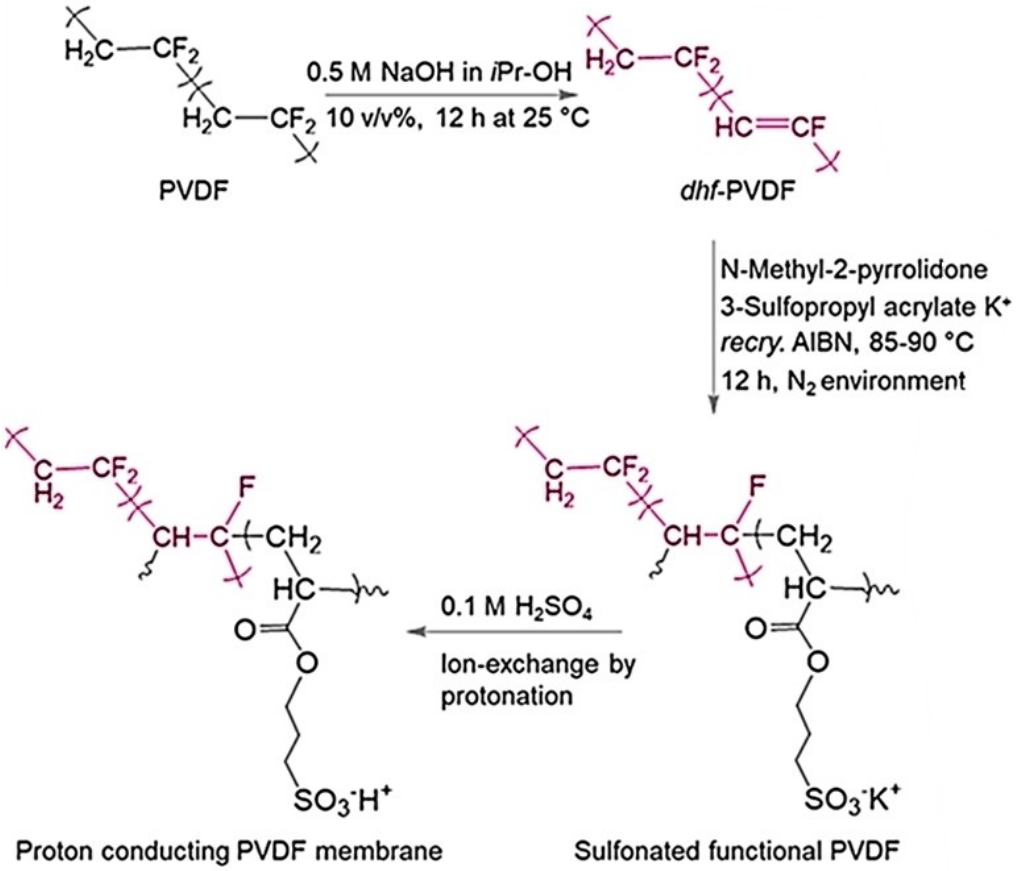

Scheme 1. Functionalization route adopted to design poly(vinylidene fluoride)-*co*-(γ)-sulfopropyl acrylate polyelectrolyte membranes in one-step one-pot manner.

Electrochemical Analysis, Ionic Conductivity and Membrane Potential

The electrochemical studies were performed using alternating current impedance spectroscopy (CH 608E, USA) in frequency range of 100 kHz–10 Hz and the membrane resistance (in Ω) was calculated from Nyquist plot (viz Re (Z′) *vs* Im (–Z′′)). The proton conductivity was calculated from specific area resistance and membrane thickness. The static transmembrane potential was probed using H-cell (SI-2) and corresponding counter-ion transport number is evaluated using the Nernst equation (Equation (1)) given below;[26]

$$t_m^+ = \frac{\left[\frac{nF \times E_{mem}}{RT \times \ln\left(\frac{[C^1]}{[C^2]}\right)}\right] + 1}{2} \quad (1)$$

Here, n = 1 (for univalent ionic charge), "F" is faradays constant (96,485 C mol^{-1}), C^1 and C^2 corresponds to the concentration of electrolytes in bi-compartment H-cell, R & T is universal gas constant (8.314 J K^{-1} mol^{-1}) and system temperature during study (T = 25 °C, 298 K), respectively.

Mechanical and Chemical Stability Analysis

The mechanical stability studies were judged from stress *vs* strain analysis using ultimate tensile testing machine (ISO 527 S2 protocol using Zwick Roell Z 2.5 tester) (Figure S2) and maximum tensile strength was calculated. The bend/flexibility tests (~180°) were also performed in doubly fold manner. The chemical durability was determined in terms of oxidative stability (Fenton's test) and by hydrolytic stability analysis of polybetaine type structures. Detailed procedures are drafted in SI-3.

Evaluation of VRF Cell Performance

For VRF cell studies, all electrochemical measurements and galvanostatic charge-discharge (GCD) were recorded with 0.25 M V^{4+}, 3 M H_2SO_4 | | 0.25 M V^{3+}, 3 M H_2SO_4 electrolyte in a serpentine carved graphite flow field with an effective area of 25 cm^2 using BTS-4008-5 V6 A-8 channel battery analyzer electrochemical workstations (Neware) at 23 ± 2 °C. Prior to cell assembly, the electrode (carbon felt (CF): 6 mm) and PVDF-*g*-SA membrane were conditioned in conc. HNO_3 and 3 M H_2SO_4, respectively. The membranes exhibit compression load of 16 ± 2% between the CF-electrodes while the electrolytes (~25 mL) were infused at a flow rate of 50 mL min^{-1} in recirculation mode using a Ravel Hi-Tech peristaltic pump (model RH–P100 S-200-2H). Furthermore, to study the influence of current density on cell performance, the rate capability experiments were evaluated between 50 mA cm^{-2}–200 mA cm^{-2} and the cell efficiencies were calculated using Equations (2)–(4)

$$\text{Coulombic efficiency (CE, \%)} = \frac{\int I_{Discharge}\, dt}{\int I_{Charge}\, dt} \times 100 \quad (2)$$

$$\text{Energy efficiency (EE, \%)} = \frac{\int V_{Discharge}\ I_{Discharge}\ dt}{\int V_{Charge}\ I_{Charge}\ dt} \times 100 \quad (3)$$

and

$$\text{Voltage efficiency (VE, \%)} = \frac{EE}{CE} \times 100 \quad (4)$$

The open circuit potential decay (i.e., self-discharge test) studies were assessed to understand the voltage holding capacity and real-time vanadium permeability trends with prepared PVDF-*g*-SA PEMs. The voltage decay rate was calculated and compared with Nafion-117 using equation (Equation (5))

$$\text{Voltage decay rate (V min}^{-1}) = \frac{\text{Total voltage drop (in V)}}{\text{Total time taken to reach 0.6 V (in min)}} \quad (5)$$

The ohmic overpotential (η^{ohm}, mV) and turnover potential (η^{t}, mV) was calculated from the charge-discharge profile at half of the theoretical capacity ($Q_{theor} = n\ F\ [V^{n+}]/3600$) and concentration overpotential region, respectively. Figure S3 illustrates the coordinates to calculate the overpotential parameters for cell with membrane employed. In addition, the influence of applied current density on membrane resistance, efficiency and capacity performance was evaluated by calculating iR drop and cyclic voltage losses. Finally, the polarization studies with optimized PVDF-*g*-SA PEMs were acquired and maximum power delivery result for single VRF cell (effective area = 6.25 cm^2) and the curves were obtained at ~100% state of charge.

2. Result and Discussion

The efficiency and operational stability of VRFB devices depend upon the transport property and selectivity of polyelectrolyte membrane (PEM).[27] For RFB applications at low pH, a separator bearing compact bulk morphologies and strongly ionizable proton conducting groups (viz $-SO_3^-$) is a preferred choice. In previous studies, the hydrocarbon polymer-based PEMs are meticulously designed due to its ease of functionalization and one-step modifications. As mentioned, a major setback which influence PEM performance is the triggered polymer scissoring from $VOO^{\bullet}$ onto the susceptible aryl-oxy motifs.[1b,5,7c] Thus, it was deemed worthwhile to investigate the fluorinated PEMs lacking aromatic functional groups in their main chains, contrasting with prior research that focused on aryl-sulfonic acid-based PEMs. (Scheme S1).

2.1. Chemical Characterization of PVDF, *d*-PVDF and PVDF-*g*-SA

After dehydrofluorination, the functional modification in pristine PVDF was confirmed using ^{1}H-NMR, ATR-IR and Raman spectroscopies (Figures 1 and S4, respectively). In ^{1}H-NMR of pristine PVDF, the shifts at 2.4 ppm and 2.9 ppm is assigned to saturated portion *viz* the tail-to-tail ($-CF_2C\underline{H}_2C\underline{H}_2CF_2-$, t) and head-to-tail ($-CH_2CF_2C\underline{H}_2CF_2-$, m) repeating units (Figure 1).[25] While the unsaturation in PVDF was evident through a new broad deshielded peak at ~5.4 ppm and 5.9 ppm (refer Section 2.2 and Figure S4a), corresponding to the –(CH=CF)– moiety.[25] To further support the double bond formation, the Raman spectrum of PVDF and *d*-PVDF were curated and the distinct and sharp peak at ~1510 cm^{-1} in *d*-PVDF confirms unsaturation.[28] Detailed deconvolution and comparative studies on PVDF and *d*-PVDF can be referred from Figure S4c. In addition, the consumption of –(CH=CF)– bond on the reaction of *d*-PVDF with γ-sulfopropyl acrylate was validated by the vanishing of peak at ~5.4 ppm and 5.9 ppm. This confers the copolymerization reaction of sulfonated acrylate monomer on to the *d*-PVDF.

Furthermore, the new peaks in PVDF-*g*-SA at 3.0–3.1 ppm and ~3.8 ppm are assigned to the $-C\underline{H}_2C\underline{H}_2-SO_3H$ and –C-(O)–O–$C\underline{H}_2$– motifs, respectively.[29] In comparison to the ATR-IR spectrum of PVDF and *d*-PVDF (Figure S4b), the new transmission bands in PVDF-*g*-SA-15 observed at 1045 cm^{-1} and 1722 cm^{-1} are assigned to the antisymmetric vibration mode of S=O ($v_{symm}^{S=O}$) bond and carbonyl group ($v^{C=O}$) from the sulfonate and ester group of the SA monomer, respectively (Figure S5).[30] In addition, a very broad inverted band between 3000–3500 cm^{-1} (which is absent in both PVDF and *d*-PVDF) corresponds to the hydrate interactions of the hydrophilic segment with water as $-SO_3H-OH_2$.[31] As expected, all the functional fingerprints from PVDF backbone and γ-sulfopropyl acrylates are preserved, hence, confirmed the successful free-radical grafting of conducting group on to the head-to-tail region of PVDF.

2.2. Morphology Imaging, Wettability Analysis and High-resolution Topology

Since vanadium electrolyte imparts gradient driven crossover, the membrane with non-porous morphology is highly desired to preserve the capacity of cell in a long-run operation. Figure 2a and b exhibit the surface and the transverse section of designed membranes. As observed, the FE-SEM images of PVDF-*g*-SA-10 and PVDF-*g*-SA-15 exhibit flawless cross-section and surface morphologies with appreciable miscibility between hydrophobic *d*-PVDF and hydrophilic γ-sulfopropyl acrylate devoid of any asymmetric pores. Moreover, the casting conditions like solvent, drying temperature, humidity and inert atmosphere played a crucial role to fabricate PEM with desired bulk attributes and surface topology (Table S1). To further confirm, the electrolyte penetration test was performed to evaluate volume transport. With PVDF-*g*-SA-10 and PVDF-*g*-SA-15, no leakage was observed in static conditions. At higher monomer concentration of 20 w/w% and above, minute leakage was observed which limited our studies up to 15 w/w% grafted PEMs only. Prima facie, such discrepancy might be due to the physical immiscibility between the hydrophobic and hydrophilic components during the reaction which crosses the reinforcement threshold limits. Furthermore, the affinity of PEMs towards water (i.e., hydrophilicity) was diagnosed using the sessile drop method in advancing mode and drop profile is

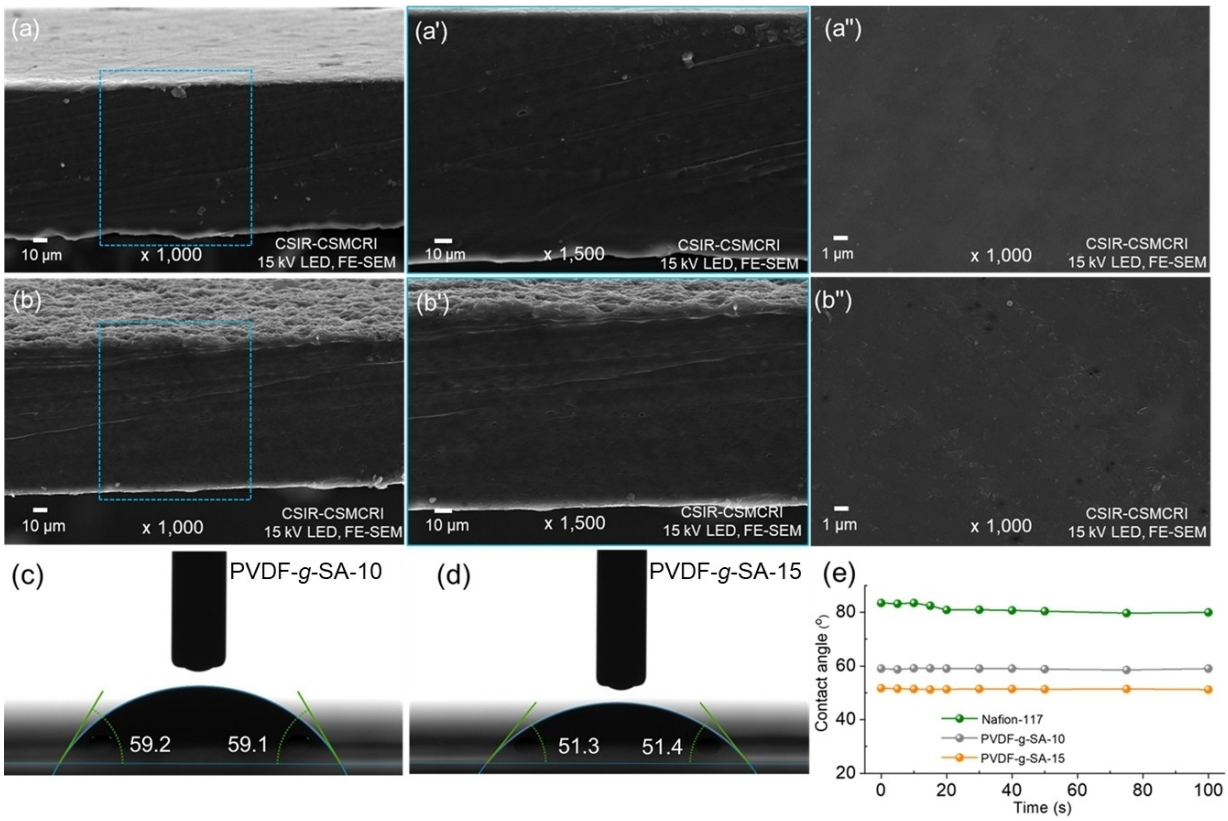

Figure 2. Field emission scanning electron microscopy imaging of poly(vinylidene fluoride)-*co*-(γ)-sulfopropyl acrylate polyelectrolyte membranes (a, a′ and a′′) PVDF-*g*-SA-10 and (b, b′ and b′′) PVDF-*g*-SA-15 showing transverse section and surface topology, (c, d) water contact angle measurement and (e) dynamic water contact angle displaying the *l-a-s* interface changes with time.

depicted in Figure 2c and d, the change in water contact angle (WCA) was also probed for 120 seconds in dynamic mode (Figure 2e). As a result, the triple-phase boundary of the membrane-electrolyte-air interface for designed PVDF-*g*-SA membranes and Nafion-117 (Figure S6) had an angle less than 90°, this suggests excellent water sorption attributes. The average contact angle was in the following decreasing order: Nafion-117 ($\theta = 84°$) > PVDF-*g*-SA-10 ($\theta = \sim 60°$) > PVDF-*g*-SA-15 ($\theta = 51°$). Hence, the hydrophilic $-(CH_2)_3-SO_3H$ groups are present in the membrane matrix for proton conduction. In addition, $\theta < 90°$ confirms that the designed membranes exhibit higher solid free surface energy (γ) and adhesion affinity (α) to electrolyte which ensure excellent proton sorption and continuous percolation. Yet, another important information from cos (θ) value obtained by static WCA measurements confers that at 15 w/w% functionalization, the hydration function is better and hence, a better proton conduction can be obtained. Similar trend was observed for the hydration number (λ) of PVDF-*g*-SA-10 and PVDF-*g*-SA-15 showing λ-values of 11 and 13, respectively.

High resolution topological feature of membranes was imaged using atomic force microscopy (AFM) in a semi-contact mode and the results were deconvoluted in terms of average surface roughness (R_{avg}) and root mean square roughness (R_{rms}) (Figure 3a and b). The R_{avg} and R_{rms} of PVDF-*g*-SA-10 and PVDF-*g*-SA-15 exhibit roughness in nanometer scale range of 1.6 to 2.6 nm and 2.6 to 3.5 nm, respectively (Figure S7). Unlike membranes bearing dented morphologies, the designed membranes can be effective in eliminating interaction with biological and fouling agents securing the lifetime of PEMs. Successively, the AFM phase study of PVDF-*g*-SA PEMs confers bi-phasic nanophase morphologies devoid of any macro/micro-phase separation (Figure 3a′ and b′). Such array of hydrophilic and hydrophobic architecture might be attributed to the significant kinetic contribution of halato-telechelic $-SO_3H$ endowed in solution phase to form well-tailored ion conducting channels.[32] Such a homogeneity in phases of PVDF and γ-sulfopropyl acrylate helps to create sub-nano channels crucial for selective proton migration over supporting bulky ions in the electrolyte medium (Figure 3c). The contrast as dark and light domains can be assigned to the low T_g phase of PVDF (hard phase) and tender hydrophilic (soft phase) SA in the PVDF-g-SA PEMs that ensures efficient water sorption and its ion dissociation in electrolyte.[33]

2.3. Fate of Water and Membrane Potential (E_{mem}) Results of PVDF-*g*-SA Membranes

Series of membranes were designed with optimum weight ratios of γ-SAK and *d*-PVDF to acquire combinatorial traits with high proton conduction and mechanical stability.[34] The phys-

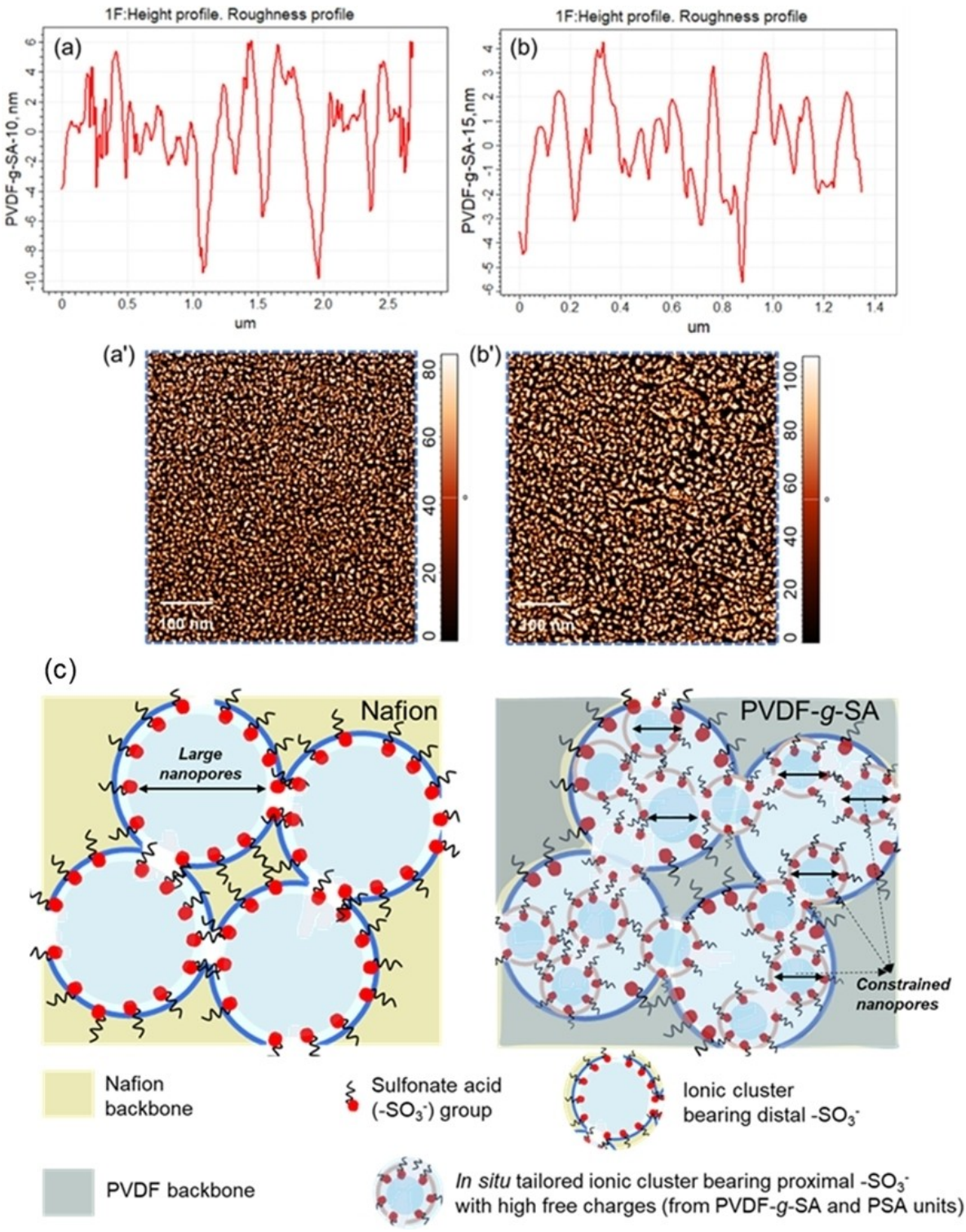

Figure 3. High resolution topography analysis of designed membranes illustrating the nano-ordered roughness profile and nanophase architectures of (a, a′) PVDF-g-SA-10 and (b, b′) PVDF-g-SA-15, respectively and (c) illustration of the ionic cluster architecture in Nafion (large percolating pores and diluted nanochannels) and designed co-polymer based membranes with some in situ tailored sulfonates for constrained percolating pores.

icochemical properties were calculated and summarized in Table 1 and results are compared to those of Nafion-117.

Acid electrolyte uptake (AEU) is essential property of PEMs, influencing ion percolation attributes and give insights related to the distribution of $-SO_3H$ groups. Generally, higher electrolyte uptake is preferred, but issues arise when it exceeds the threshold, leading to charge dilution.[35] An optimum electrolyte uptake in PEMs ensures better ion dissociation and improves ion diffusivity desired for high electrochemical traits.[36] For designed membranes, the AEU was proportional to the func-

Table 1. Physicochemical properties and vanadium uptake attributes of prepared poly(vinylidene fluoride)-*co*-(γ)-sulfopropyl acrylate polyelectrolyte membranes and comparison with those of Nafion-117 in similar conditions.

Membrane nomenclature	Acid electrolyte uptake (AEU, %)[a]	Volumetric swelling (SR, %)[a]	Liner expansion ratio (LER, %)[a]	Ion-exchange capacity (IEC, meq g^{-1})[a]	Vanadium ion uptake (VIU, %)[b]
PVDF-*g*-SA-10[c]	19 ± 3	8.5 ± 2	6 ± 1	0.9 ± 0.2	4.0 ± 0.5
PVDF-*g*-SA-15[c]	28 ± 5	13.5 ± 2	6.7 ± 1	1.2 ± 0.2	6.8 ± 0.5
PVDF-g-SA-20[c]	36 ± 5	17 ± 2	8.2 ± 1	1.4 ± 0.2	12.5 ± 1.0
Nafion-117	30 ± 2	10 ± 2	6 ± 1	1.4 ± 0.2	9.5 ± 0.5

Note: [a] Evaluated in 3 M H_2SO_4 and [b] Evaluated in 1 M $VOSO_4$ | 3 M H_2SO_4 electrolyte and calculated using equation; VIU = [(W_{mem}^{V4+} − $W_{mem}^{Acid\ elec.}$)/W_{mem}^{dry}]*100 at 25 °C. [c] = polyelectrolyte membrane thickness ~150 μm.

tional grafting of the sulfonated acrylate in the following decreasing order: PVDF-*g*-SA-20 (36 ± 5 %) > PVDF-*g*-SA-15 (28 ± 5 %) > PVDF-*g*-SA-10 (20 ± 3 %). Furthermore, the AEU and ion-exchange capacities (IEC) of PEM illustrates the proportional relation. For designed PEMs, the highest IEC obtained was 1.47 ± 0.2 meq g^{-1} at 20 w/w% grafting whilst PVDF-*g*-SA-15 and PVDF-*g*-SA-10 exhibit 1.23 ± 0.2 meq g^{-1} and 0.91 ± 0.2 meq g^{-1} of IEC, respectively. However, at 20 w/w% grafting, the homogeneity in PEM was compromised during temperature-induced phase inversion (Figure S8), rendering it inappropriate for further application.

To study the dimensional stabilities, volumetric expansion ratio (VER) and linear expansion ratios (LER) were calculated. From the analysis, the expansion resistance attributes were in order: PVDF-*g*-SA-10 (6 ± 1 %) > PVDF-*g*-SA-15 (~6.5 ± 1 %) > PVDF-*g*-SA-20 (~8 ± 5 %) where the higher bulk water sorption in PEM matrix by γ-sulfopropyl acrylate moieties. Moreover, the penetration of vanadium ions in PEM is undesired. Such behaviour might speed-up the crossover of vanadium ions and can offend the VRFB performance.[37] Thus, lowest possible vanadium ion uptake (VIU) is desired. The VIU was in increasing order: PVDF-*g*-SA-10 (~4.0 ± 0.5 %) < PVDF-*g*-SA-15 (~7.0 ± 0.5 %) < PVDF-*g*-SA-20 (~12.5 ± 1.0 %) which is directly correlating with concentration of sulfonic acid groups as confirmed by IEC. Furthermore, the membrane potential was investigated to understand the counter-ion transport affinity and compared to that of Nafion-117. The transport number (t_{sodium}^{+}) trend of PVDF-*g*-SA PEMs affirms conductivity result and exhibits t_{sodium}^{+} > 90 %, and hence designed PEMs could be of high interest to exploit its fate in VRFBs.

2.4. Electrochemical Properties: Conductivity, Influence of VO^{2+}-ions on PVDF-*g*-SA Property and *i-V* Characteristics

Electrochemical properties were deduced from Nyquist plots, Bode-phase analysis and current-voltage responses to gain insights into ion conducting properties (Figure 4). The qualitative analysis of AC-impedance response for designed membranes and Nafion-117 confers a complex conductivity behaviour showing three well-defined curves viz at higher frequency, intermediate frequency and lower frequency regions assigned for the cell resistance, ion-transfer resistance and Warburg-diffusion resistance, respectively (Figure S9).[6b,9b,26] When operated in 0.25 M $VOSO_4$; 3 M H_2SO_4 electrolyte, the Nafion-117 exhibits an overall cell resistance (R_{cell}) of 86 mΩ whilst the PVDF-*g*-SA-10, PVDF-*g*-SA-15 and PVDF-*g*-SA-20 impart cell resistance of ~100 mΩ, 87 mΩ and 68 mΩ, respectively. However, in 3 M H_2SO_4 electrolyte, the R_{cell} was in following decreasing order; PVDF-*g*-SA-10 (53 mΩ) > PVDF-*g*-SA-15 (41 mΩ) > Nafion-117 (39 mΩ) > PVDF-*g*-SA-20 (32 mΩ). This dramatic lowering of resistance by approx. two orders in magnitude can be explained based on the van der Waal volume of counter-ions (an electrostatic binding parameter which dictates ion mobility) and perturbations in the nanostructure of ionic domains under the influence of variable ion constrains.[38] Furthermore, the impact of solution composition was evidenced in the semi-circular region of high-resolution Re (Z′) *vs*–Im (Z″) (Figure S9) which simplify our understanding to navigate the electrochemical properties considerably depends on the hydration free energy of counter-ions in electrolyte solution.[39] Figure 4b represents the Bode-phase analysis for Nafion-117 and as prepared PVDF-*g*-SA membranes. From spectrum, we culminate that the ion-conduction phenomena of commercially available PFSA membrane and PVDF-*g*-SA are identical and transports either through Grotthuss mechanism, site-hopping or vehicular mechanism.[40] The proton conductivity of Nafion-117 and PVDF-*g*-SA membranes in 3 M H_2SO_4 electrolyte at 25 °C was ~18.8 mS cm^{-1} and between 11 to 17 mS cm^{-1}, respectively. However, the ionic conductivity (from mutually co-existing H^+ and VO^{2+}) of PVDF-*g*-SA membranes changed in real-time vanadium electrolyte and ranged between 6 to ~9 mS cm^{-1} whilst the Nafion-117 possess 9.5 mS cm^{-1} (Table 2). Since, PVDF-*g*-SA-15 exhibits an optimum balance between AEU, IEC, VIU and κ_m^{H+}, the results infer that it can be a competitive PEM material to Nafion-117.

The current *vs* voltage was curated in dry and wet conditions of PEMs to understand the ion gating behaviour (Figure 4c and d). The PEMs exhibit blockage type response and asymmetric diode type response for dry and wet membrane conditions, respectively. As a fact, the membranes in wet state are showing rectification behaviour where the ions percolate through the nanochannels made by sulfonate functionalities whilst the ion mobility was impeded in dry state attributed to inconsistencies and drying (loss in bound water continuity) experienced by the PEMs. Interestingly, the ion gating and cell

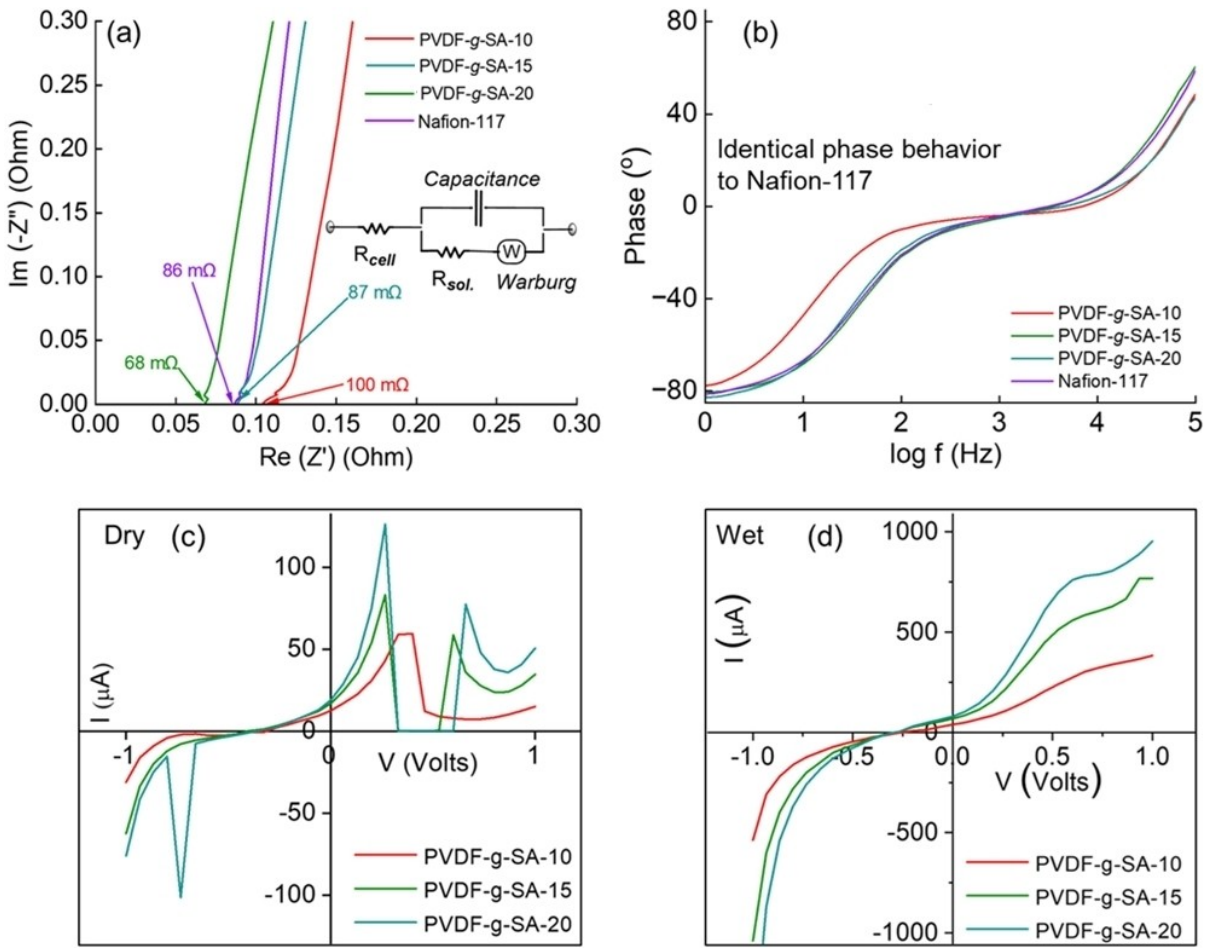

Figure 4. Electrochemical analysis of the PVDF-*g*-SA and Nafion-117 membranes; (a) Nyquist plots of the PEMs in 0.25 M VO^{2+} | ($-SO_3^-H^+$ $_{solid}$) | 3.0 M H_2SO_4 at 25 °C (inset: showing the Randle's circuit used to fit the impedance spectrum), (b) bode-phase plot displaying the ion conduction behaviour, (c–d) current *vs* voltage curves of the membranes in bias range of −1 V to +1 V (c) dry state (conditioned in 3 M H_2SO_4 electrolyte and wiped) and (d) wet state (3 M H_2SO_4).

Table 2. Influence of electrolyte medium on the ion conductivity properties of poly(vinylidene fluoride)-co-(γ)-sulfopropyl acrylate polyelectrolyte membranes and its comparison with Nafion-117 in similar conditions.

Membrane nomenclature	κ^m, H^+ (mS cm^{-1})[a]	κ^m, H^+/V^{4+} (mS cm^{-1})[b]	t_{sodium}^+ (%) (0.1 NaCl | | 0.01 NaCl, 25 °C)
PVDF-*g*-SA-10	11.0 ± 0.5	6.0 ± 0.5	87 ± 1
PVDF-*g*-SA-15	17.0 ± 0.5	7.0 ± 0.5	91 ± 1
PVDF-g-SA-20	14.5 ± 0.5	8.8 ± 0.5	91 ± 1
Nafion-117	18.8 ± 0.5	~ 9.5 ± 0.5	93 ± 1

Note: [a] Evaluated in 3 M H_2SO_4 and [b] evaluated in 1 M $VOSO_4$ | 3 M H_2SO_4 electrolyte at 25 °C.

resistance mutually agrees for the desired electrochemical properties for proton percolation.[41]

2.5. Chemical and Mechanical Stabilities of PVDF-*g*-SA Membrane

Ensuring stable long-run performances and high operational life of the VRF cell, the designed membrane should possess excellent resistance to oxidative/chemical degradation. The oxidative and hydrolytic durability analysis were performed in Fenton's reagent and 3 M H_2SO_4, respectively (**SI-3**) and the results are shown in Figure 5a and c. In conventional hydrocarbon-based PEMs e.g., s-PEEK and polystyrene sulfonates, the oxidative species cleaves the polymer chain via triggered dynamics.[5b,7c] In contrast, the fluorinated proton exchange membranes bearing durable C–F bonds exhibit excellent resistance to polymer scissoring.[6a] As displayed in Figure 5b, due to high absorption of vanadium during charging stage, the rate of degradation increases attributed to higher $VOO^{\bullet}$ generation. Moreover, with PVDF-*g*-SA PEM, the penetration of VO_2^+ can be reduced by the hydrophobic PVDF hence, ensuring

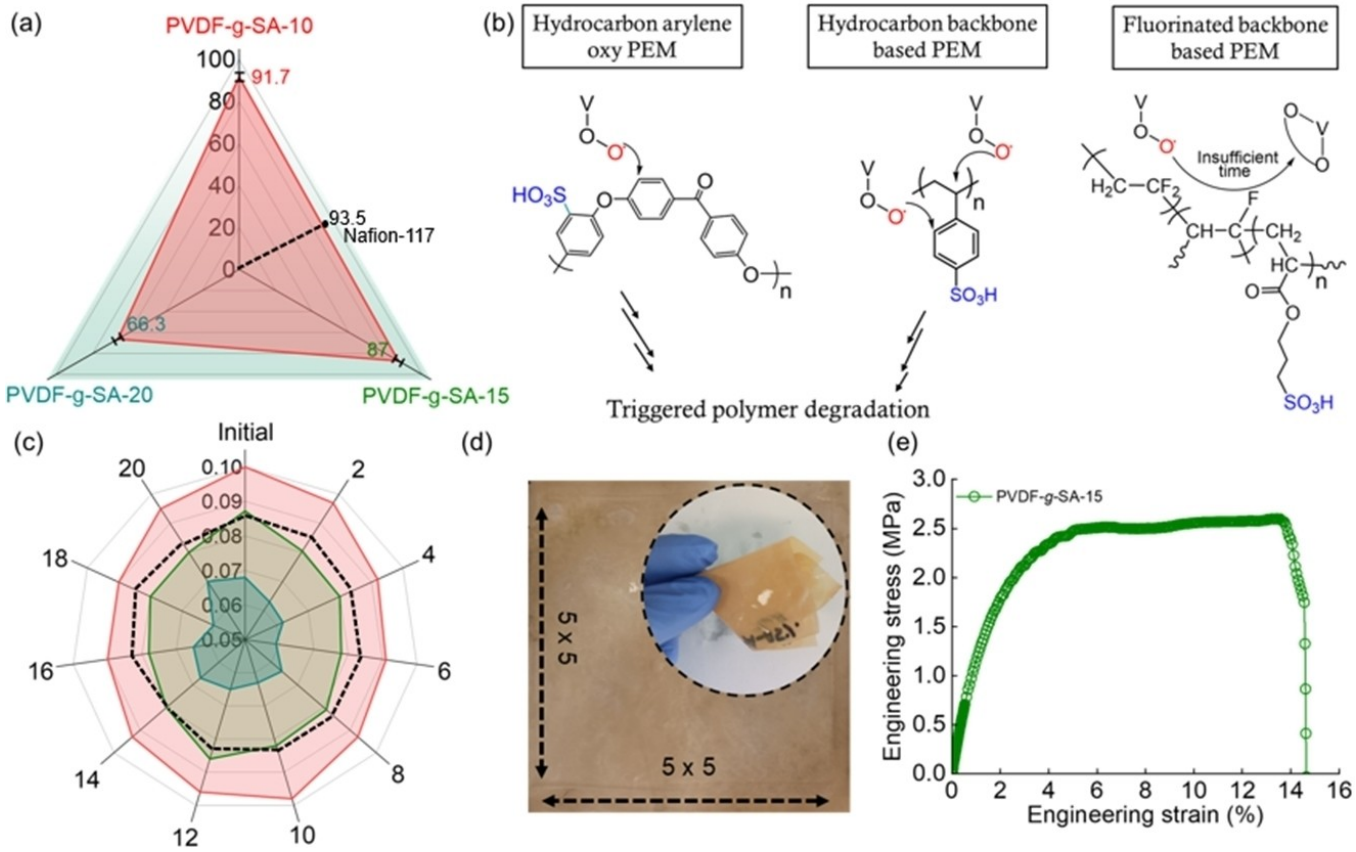

Figure 5. Stability analysis and performance retention of PVDF-*g*-SA-15 PEM; (a) Fenton's oxidative stability showing the percentage ionic conductivity retention after 72 h of immersion time, (b) plausible mechanism for the oxidative stability and its mechanistic comparison with conventional hydrocarbon backbone and resistance mechanism in fluorinated PEM, (c) hydrolytic stability for 22 d evidencing membrane resistance in 3 M H_2SO_4 at 25 °C (dotted: Nafion-117 standard, ~180 μm), (d) optical image of the membrane (dimensions in cm) after testing and, (e) ultimate tensile testing (stress vs strain curve taken over vertical stretching rate of 2 mm s^{-1}) at 25 °C for hydrated PVDF-*g*-SA-15 PEM of 150 μm.

stability. As highlighted from Figure 5a, bearing 10 w/w%, 15 w/w% and 20 w/w% of γ-sulfopropyl acrylate, the PVDF-*g*-SA membrane retained ~92%, 87% and 66% of its initial κ_m^{H+}, respectively. This evidences that with higher sulfonic acid group, the bulk orientation of functionalities is more prone to degradation due to the expected cleavage of ester functions and not by PVDF (since its mechanical stability was retained as confirmed by 180° bend test, Figure 5d). Furthermore, the hydrolytic stability was performed in 3 M sulphuric acid for 20 days. Surprisingly, the results for hydrolytic stability of all PVDF-*g*-SA PEMs illustrate >95% conductivity retention (Figure 5c). A plausible explanation to such unprecedented stability at low pH of these sulfabetaine-type structure underlies the stabilization of acrylates by proton delocalization from α-position. This detailed mechanism showing functional interconversion of ester groups to enol-ethers is highlighted in Scheme S2. In addition, such systems can induce ancillary conducting groups for proton migration as enol-ethers (=C-(OR)–OH) or carboxylates (–COO^-).[39b] These results are consistent with the extraordinary stability reported by Schönemann et al. and Zhao et al.[42]

Finally, the mechanical stability of shortlisted PVDF-*g*-SA-15 was examined from engineering stress *vs* engineering strain curve obtained using universal testing machine (Figure 5e). The curve suggests an excellent tenacity of the PEM material attributed to the good mechanical properties of PVDF and bound water plasticization reinforcement.[43] Successively, two regions viz. the proportional plastic deformation, smooth elastic point with strain hardening region confers that, these materials are tough (T_{max} = 2.5 MPa) and flexible (E_{break} = 14%) enough to sustain compression loads of electrodes in RFB cell.

2.6. Rechargeable Vanadium Flow Cell Performance

The motivation of this work is to design a cheaper alternate fluorinated polyelectrolyte membrane mimicking the chemical structure of Nafion and to achieve desired efficiencies, capacity and stability in long-run. Thus, to evaluate real-time performance, the designed PVDF-*g*-SA-15 and Nafion-117 were assembled in VRF cell (details in the experimental section) and in-situ stability and performance studies were curated in terms of self-discharge analysis (open circuit voltage [OCV] profiling), galvanostatic charge-discharge (GCD), rate-capabilities (to understand the influence on overpotential/efficiency and iR-

drop of cell) and peak power delivery from polarization plot (Figures 6–8).

2.6.1. Self-discharge Analysis

To comparatively understand the in-situ crossover attributes and difference in vanadium migration aptitude of PVDF-*g*-SA-15 and Nafion-117, the self-discharge analysis was performed (Figure 6). The voltage drop curve manifests asymptotical nature, which means that the cell experiences OCV decay attaining peak charge potential (i.e., 1.8 V) and progressively tapers off with time, showing distinct losses. On comparing the results, the PVDF-*g*-SA-15 sustained the concordant voltage of 1.42 V for 750 min whilst the Nafion-117 holds 1.40 V for 370 min, only. This suggests that the vanadium permeability of Nafion-117 during operation is approx. 2 times higher in magnitude when compared to designed PVDF membrane. Moreover, the voltage drop rates calculated for Nafion-117 and PVDF-*g*-SA-15 were 2.56×10^{-3} V min^{-1} and 1.37×10^{-3} V min^{-1}, respectively. Consequently, the ionic architecture of PVDF-*g*-SA-15 is much smaller and random than Nafion-117 which exists as reverse micelle assembly bearing large swollen percolating channels. In addition, these results were in very good affirmation to vanadium ion-uptake (VIU) results obtained during the preliminary phase of physicochemical analysis, where the VIU for Nafion-117 was 28% higher than that of PVDF-*g*-SA-15. Thus, these results confer that the fabricated PVDF-*g*-SA-15 can be used for the rate capability experiments and long-run GCD cycling.

2.6.2. Specific Capacity of VRF Cell with PVDF Based PEM

Initial investigation on the specific capacity delivery was exploited at 50 mA cm^{-2} of operational current density. Figure 7a depicts the alpha curve showing charge-discharge behaviour of as prepared PVDF-*g*-SA-15 and commercial PEMs. As the results, Nafion-117 exhibits overpotential (η) of 264 mV whilst PVDF-*g*-SA-15 displayed 273 mV. The obtained specific capacities (Q) were in the increasing order: Nafion-117 (5.6 Ah L^{-1}) < PVDF-*g*-SA-15 (6.6 Ah L^{-1}) which is 85% and 98.5% of theoretical Q ($Q_{theor.}$ = 6.7 Ah L^{-1}), respectively. The observed specific capacity experienced by the device is in close correlation to the membrane wettability. Wettability played a crucial role where the cosθ values (a determinant of electrolyte adhesion affinity, ‹α› and high surface free energy, ‹γ›) were in the decreasing order: PVDF-*g*-SA-15 [cos(60°) = +0.50] > Nafion-117 [cos(80°) = +0.17] which ensures a selective H^+ exchange property in PVDF-*g*-SA PEMs.

2.6.3. Efficiency and Rate Capability of VRF Cell with PVDF Based PEM

The efficiency parameters like coulombic efficiency (CE), voltage efficiency (VE) and energy efficiency (EE) at 50 mA cm^{-2} for Nafion-117 was 95.5%, 78%, and ~76%, while for PVDF-*g*-SA-15 values were 95%, ~81% and ~77%, respectively (Figure 7c and d). Despite lower η-value of PFSA membrane, the EE of PVDF-*g*-SA-15 was nearly 3% higher and was compensated by lower permeability of vanadium which achieved higher CE than

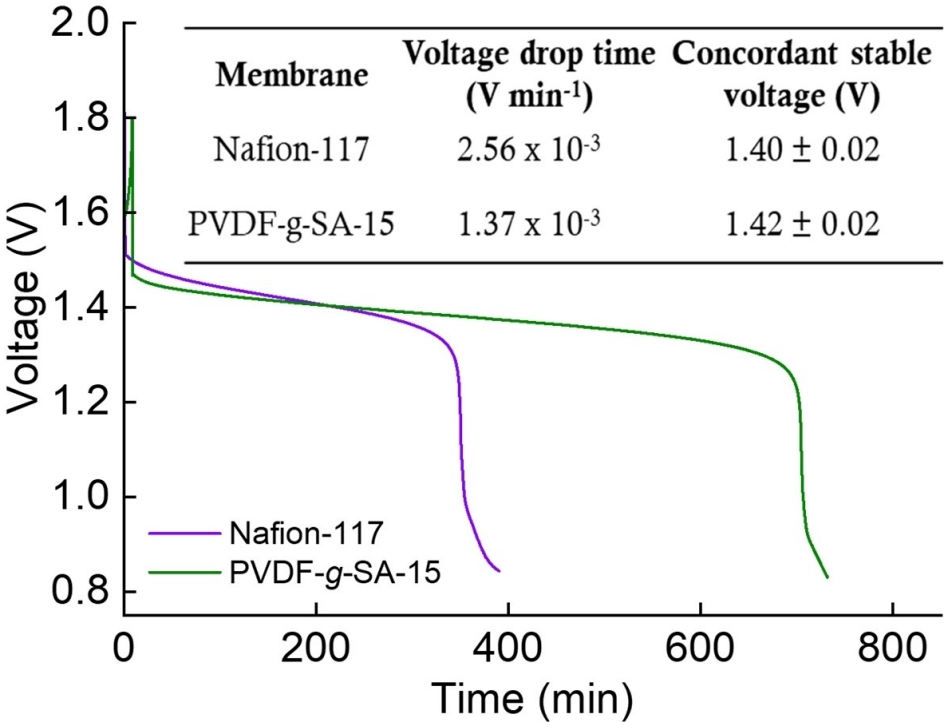

Figure 6. Self-discharge analysis showing open circuit voltage (OCV) decay of PVDF-*g*-SA and its comparison with Nafion-117 using 0.25 M redoxolyte concentration.

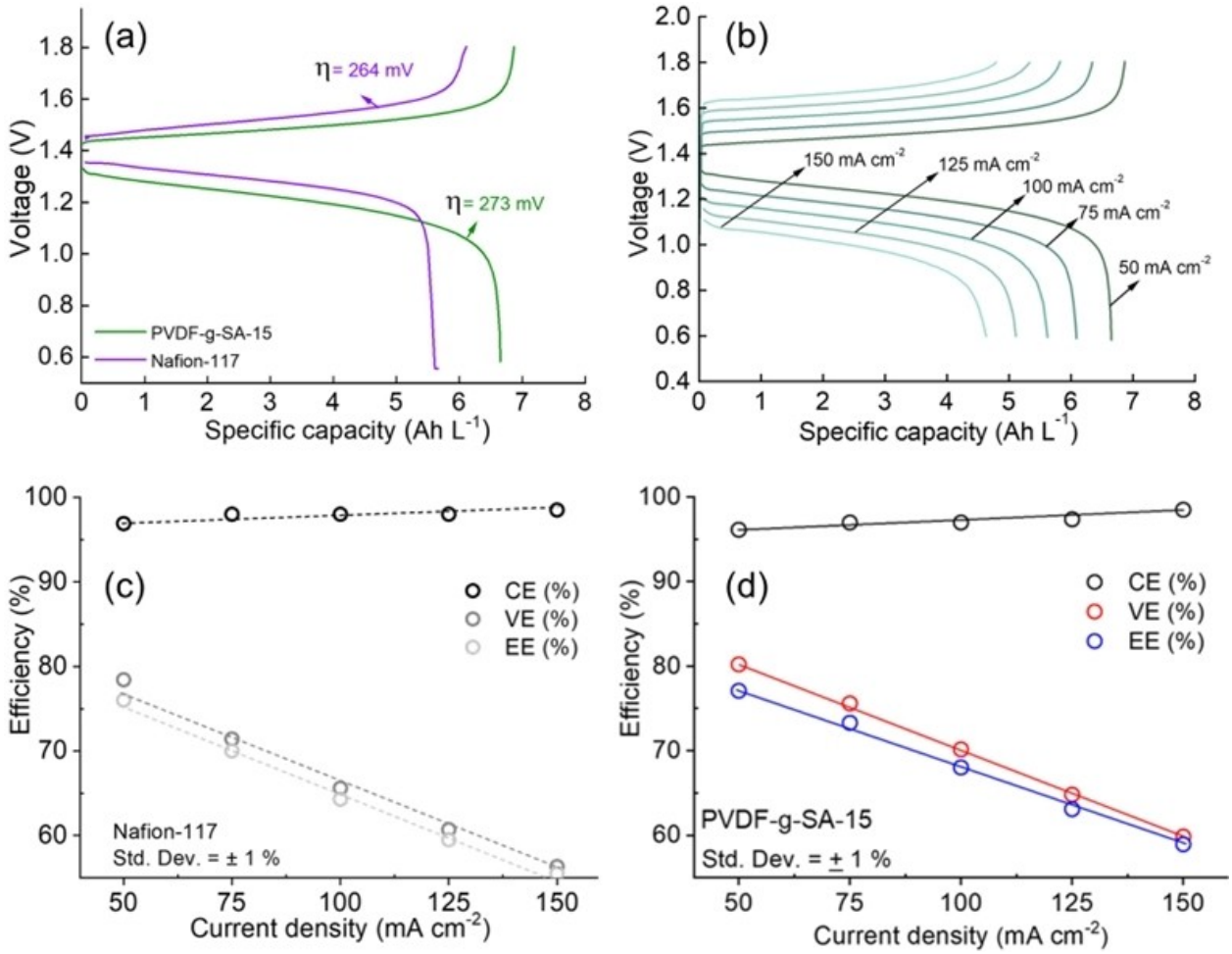

Figure 7. Flow cell performance; (a) galvanostatic charge-discharge (GCD) analysis of PVDF-*g*-SA-15 and Nafion-117 at 50 mA cm^{-2}, (b) rate-capability GCD experiments for PVDF-*g*-SA-15, (c) efficiency trends of (c) Nafion-117 and (d) PVDF-*g*-SA-15.

Nafion-117. A rational correlation can be made with the Nyquist plots of both the membranes where at higher frequencies, the area normalized resistance of Nafion-117 is lower (2.15 Ω cm^2) than that of PVDF-*g*-SA-15 (2.18 Ω cm^2). However, at lower frequencies near the Warburg region (diffusion-based region), the trend gets reversed, and polarization is prominent for PVDF-*g*-SA-15 membrane (Figure 7a and c). The rate capability analysis was performed to study the influence of applied current density on efficiency and specific capacity (Figure 7b and d). With increasing current density in order 50, 75, 100, 125 and 150 mA cm^{-2}, the CE value increased from 95% to 98.5% whilst, the VE and EE decreased from 81% to 60% and 77% to 59%, respectively.. In addition, the PVDF-*g*-SA-15 membranes stably sustained the efficiencies for 50 GCD cycles during rate capability experiments (Figure S10).

2.6.4. Long-run Performance and Polarization Curve

Finally, the studies were corroborated for long-run applicability in VRFBs by operating at 150 mA cm^{-2} for 150 continuous GCD cycles (Figure 8a and b). With designed membranes, the efficiencies were found stable with a slight VE decay in the beginning attributed to concentration polarization effect and thereafter becomes stable. Moreover, the capacity retention profile (Figure 8c) illustrates that the PVDF-*g*-SA-15 retains 40% of its initial capacities whereas, Nafion-117 hold below 10% suggesting better life of VRF cell with new PVDF based PEMs. Besides, considering the real scenario, for instance, not all circumstances result in symmetric charge and discharge currents. Depending upon the load requirements from VRFBs, the charge and discharge current densities may vary. Thus, asymmetric current density incurred charge-discharge profile can be visualized from rate capability results to understand the performance efficacy over higher or lower current drag demands. For representative case, at I_{charge} = 150 mA cm^{-2}, the charge to discharge specific capacity ratio increased by ~30% from 0.97 to 1.06 to 1.17 to 1.27 and to 1.38 for $I_{discharge}$ = 150, 125, 100, 75, 50 mA cm^{-2}, respectively.

These motivating results suggest that, even if cell is fast charged at high current density, the PVDF-*g*-SA-15 PEM assembled cell can deliver stable discharge capacities at any range of lower $I_{discharge}$ for longer period. Finally, the polarization studies were performed at ~100% state-of-charge to obtain

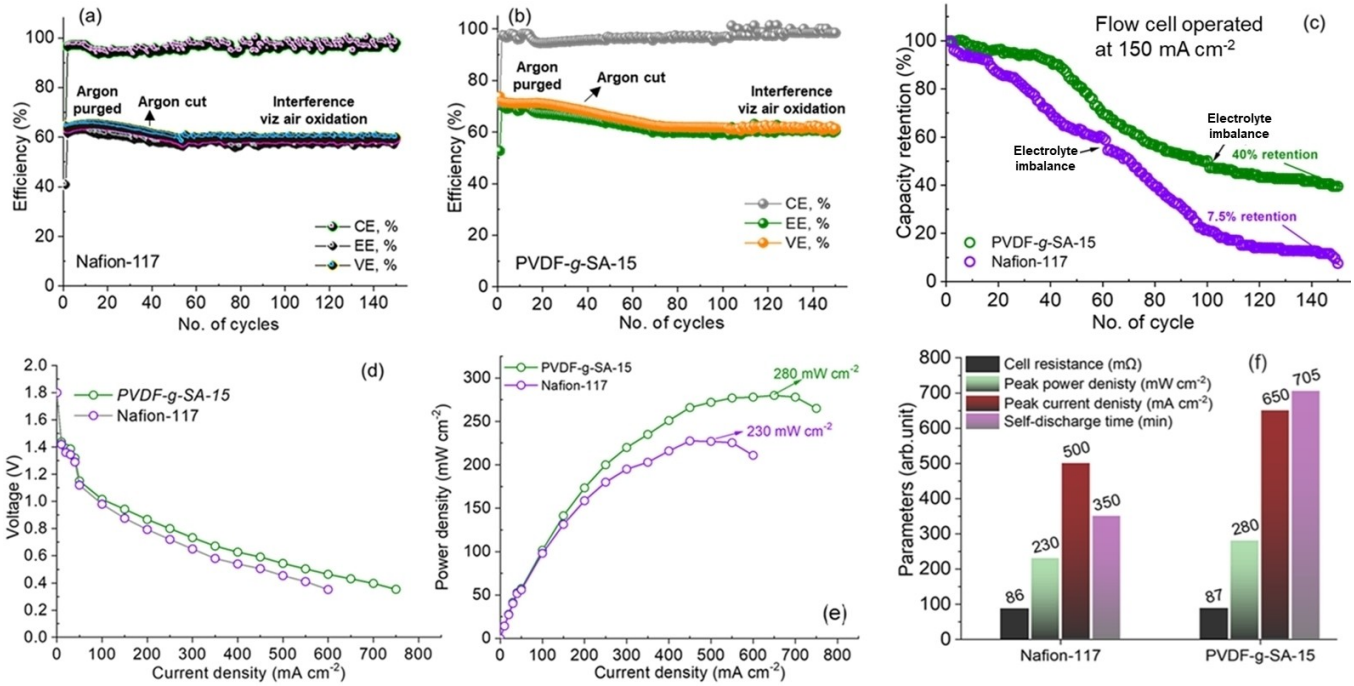

Figure 8. Long-run vanadium redox flow cell testing at 150 mA cm^{-2} (a) Nafion-117, (b) PVDF-*g*-SA-15 membrane, (c) capacity retention profile comparison, (d) polarization curve showing voltage losses during current intake, (e) peak power density achieved using designed membrane and its comparison with Nafion-117 (electrolyte composition: 0.25 M $VOSO_4$ | | 3 M H_2SO_4), and (f) correlation of peak power density and peak current density with cell resistance and self-discharge time (CE, VE and EE stand for coulombic efficiency, voltage efficiency and energy efficiency, respectively).

peak power density using the best performing PVDF-*g*-SA-15 and compared to Nafion-117 (Figure 8d–f). The obtained polarization curve (Figure 8d) illustrates three distinct regions corresponding to the activation loss (1.8 V to 1.45 V, V^{act}), concentration polarization loss (1.45 V to 0.65 V, V^{Pol}) and mass transfer loss (0.65 V to 0.40 V, V^{mt}). From observations, the PVDF-*g*-SA-15 delivers excellent peak power density of 280 mW cm^{-2} at a peak current density of 650 mA cm^{-2}. In contrast, the Nafion-117 exhibits 230 mW cm^{-2} at a peak current density of 500 mA cm^{-2} (Figure 8e). On comparing the impedance results, we expected almost the same peak power density since the internal cell resistance is ~85 mΩ. Such a behaviour could be explained based on the difference in mass transfer region of polarization curve where the voltage drop is rapid for Nafion-117 while transfer resistance dominates. Figure 8f depicts the comparative performance between PVDF-g-SA-15 and Nafion-117 membranes, focusing on parameters such as cell resistance, peak power density, peak current density, and self-discharge time. Further analyses were performed to determine functional group changes using ATR-IR and Vanadium ion uptake (VIU) after 150 continuous VRF cell cycling in PVDF-*g*-SA-15 membrane (Figure S11). As observed, attributed to the reinforcement from the all fluoro-alkyl backbone, the functional identity remained unchanged. Moreover, a minute increment in VIU was observed and this might be attributed to the bulk absorption of the vanadium electrolyte during long-run operations. These results suggest robust chemical structure of membranes under vanadium redox flow operations. As observed, the PVDF-*g*-SA-15 material have competitive performance results in comparison to Nafion-117 for VRFB application.

3. Conclusions

A fluorinated proton exchange membrane with halato-telechelic architecture is fabricated via simple graft copolymerization of γ-sulfopropyl acrylate potassium salt onto the dehydrofluorinated PVDF (*d*-PVDF). Results suggest that the stability of designed PVDF-*g*-SA PEM in oxidative environment is due to the reinforcement from fluorinated PVDF backbone and retains ~87% of initial κ_m after Fenton's oxidative stability test. Static contact angle measurements confer that the electrolyte adhesion affinity of PVDF-*g*-SA ($\theta = \sim 60°$) is much higher than that of Nafion-117 ($\theta = 80°$) and hence, can assist carbon electrodes to better utilize the redox species during charge-discharging (14% higher than Nafion-117). Moreover, the surprising and unprecedented hydrolytic stability of acrylate monomer (viz. the ester group) after copolymerization with *d*-PVDF may be explained based on variable stabilization effects like the α-proton activation effect (delocalization induced stabilization in polyesters). However, it is believed that a cognitive insight on the stability prospect of PVDF-*g*-SA membranes is still needed to be addressed through novel spectroscopic techniques. As evidenced by phase imaging and self-discharge analysis with randomly oriented halato-telechelic architectures, the vanadium crossover can be suppressed by ~2 times in comparison to that of Nafion-117 bearing oriented

reverse micelle architectures. During long-run at 150 mA cm^{-2}, the proposed membrane retained >95% of efficiency without compromising its mechanical integrity. In addition, polarization studies revealed that the optimized PVDF-*g*-SA membrane (~150 μm) delivered ~18% higher power density than Nafion-117 (~180 μm) did. A critical care on its environment sensitivity during casting is explored, the fabrication requires highly dry conditions (<20% RH) and moderate hydrophilic monomer concentration. We believe that PVDF-*g*-SA PEM can be a potential candidate for up-scaling opportunities for VRFB's. Our future emphasise underlies overcoming the trade-offs between high sulfonic acid functionalities and bi-phasic nanophase miscibility and to validate proposed stability mechanism with high capacity retention and cyclability during energy storage applications.

Associated Content: Supporting Information File

Supporting Information is available from the Wiley Online Library or from the author at Detailed procedures to calculate the physicochemical and electrochemical traits of PEMs; table showing the influence of processing solvent on membranes bulk property. ^{1}H spectra of PVDF and *d*-PVDF, and Raman spectra of PVDF and *d*-PVDF; ATR-IR spectra of PVDF-*g*-SA; AFM topology images of PVDF-*g*-SA PEMs; optical images of the fabricated membranes; contact angle of PVDF, Nafion-117 and PVDF-*g*-SA membranes, efficiency profile for 50 cycle rate capability experiment and post-mortem analysis of the PVDF-*g*-SA-15 membrane.

Acknowledgements

B. A thank the French Fluorine Network (Groupement d'Intérêt Scientifique, GIS) and PEPR Programme (ANR −22 –PEPR Recyclage −0008, Nouvelles Technologies de l'Energie). J. S acknowledges Indo-French Centre for the Promotion of Advanced Research (IFCPAR/CEFIPRA) and French National Center for Scientific Research (CNRS) for the financial and laboratory support under the Raman-Charpak Fellowship (RCF) program [OM offer no.: IFC//4141/RCF 2022/375 *w.e.f.* 02/2023], University Grant Commission, New Delhi for Junior/Senior Research Fellowship (UGC, File No. 191620048179 *w.e.f.* 08/2020) and Dr. Vikrant Yadav (JSPS Fellow at University of Yamanashi, Japan) for his useful discussions. V. K and J. S thank Centralized Instrumentation Facility (CIF) of CSIR-Central Salt and Marine Chemicals Research Institute (CSIR-CSMCRI) for advanced instrumental support. CSIR-CSMCRI communication number 44/2024.

Conflict of Interests

The authors declare no conflict of interest.

Data Availability Statement

The data that support the findings of this study are available in the supplementary material of this article.

Keywords: Electrochemical energy storage · Long-side chain structures · Membranes · PVDF copolymers · Redox flow batteries

[1] a) B. G. Thiam, S. Vaudreuil, *J. Electrochem. Soc.* **2021**, *168*, 070553; b) J. Sharma, V. Kulshrestha, *Results Chem.* **2023**, *5*, 100892; c) United Nations Framework Convention on Climate Change (UNFCCC), United Nation 2018.
[2] a) W. Lu, X. Li, *Acc. Mater. Res.* **2023**, *4*, 681–692; b) K. Amini, A. N. Shocron, M. E. Suss, M. J. Aziz, *ACS Energy Lett.* **2023**, *8*, 3526–3535; c) P. Arévalo-Cid, P. Dias, A. Mendes, J. Azevedo, *Sustain. Energy Fuels* **2021**, *5*, 5366–5419; d) S. Ebner, S. Spirk, T. Stern, C. Mair-Bauernfeind, *ChemSusChem* **2023**, *16*, e202201818; e) C. Zhang, L. Zhang, Y. Ding, S. Peng, X. Guo, Y. Zhao, G. He, G. Yu, *Energy Storage Mater.* **2018**, *15*, 324–350.
[3] H. Zhang, W. Lu, X. Li, *Electrochem. Energy Rev.* **2019**, *2*, 492–506.
[4] a) P. C. Ghimire, A. Bhattaraj, N. Wai, T. M. Lim, *Flow Batteries* **2023**, ch.25, pp. 589–606, DOI: 10.1002/9783527832767; b) Á. Cunha, J. Martins, N. Rodrigues, F. P. Brito, *Int. J. Energy Res.* **2015**, *39*, 889–918.
[5] a) S. H. Hong, M. S. Cha, S.-K. Hong, S.-G. Oh, J. Y. Lee, *ACS Sustain. Chem. Eng.* **2019**, *7*, 17088–17099; b) S. Kim, T. B. Tighe, B. Schwenzer, J. Yan, J. Zhang, J. Liu, Z. Yang, M. A. Hickner, *J. Appl. Electrochem.* **2011**, *41*, 1201–1213.
[6] a) K. A. Mauritz, R. B. Moore, *Chem. Rev.* **2004**, *104*, 4535–4586; b) A. Kusoglu, A. Z. Weber, *Chem. Rev.* **2017**, *117*, 987–1104.
[7] a) N. Zhao, A. Platt, H. Riley, R. Qiao, R. Neagu, Z. Shi, *J. Energy Storage* **2023**, *72*, 108321; b) T. Ji, C. Zhang, X. Xiao, Y. Wang, D. Cao, A. Adomkevicius, Y. Zhao, X. Sun, K. Fu, H. Zhu, *Small* **2023**, *19*, 2206807; c) D. Chen, M. A. Hickner, *Phys. Chem. Chem. Phys.* **2013**, *15*, 11299–11305.
[8] a) B. Jiang, L. Wu, L. Yu, X. Qiu, J. Xi, *J. Membr. Sci.* **2016**, *510*, 18–26; b) B. Jiang, L. Yu, L. Wu, D. Mu, L. Liu, J. Xi, X. Qiu, *ACS Appl. Mater. Interfaces* **2016**, *8*, 12228–12238.
[9] a) C. M. Pawar, S. Sreenath, B. Bhatt, D. Y. Nikumbe, W. F. G. Saleha, R. K. Nagarale, *Colloids Surf., A* **2023**, *667*, 131295; b) J. Sharma, H. Khan, P. Upadhyay, R. Kothandaraman, V. Kulshrestha, *ACS Appl. Energy Mater.* **2023**, *6*, 447–460.
[10] a) D. Zhang, Z. Xu, X. Zhang, L. Zhao, Y. Zhao, S. Wang, W. Liu, X. Che, J. Yang, J. Liu, C. Yan, *ACS Appl. Mater. Interfaces* **2021**, *13*, 4051–4061; b) P. Qian, W. Zhou, Y. Zhang, D. Chao, M. Song, *Energy Fuels* **2023**, DOI: 10.1021/acs.energyfuels.3c02373.
[11] a) J. Li, Y. Zhang, S. Zhang, X. Huang, *J. Membr. Sci.* **2015**, *490*, 179–189; b) R. Niu, L. Kong, L. Zheng, H. Wang, H. Shi, *J. Membr. Sci.* **2017**, *525*, 220–228; c) J. Sharma, P. Upadhyay, S. Mishra, V. Kulshrestha, *Int. J. Hydrogen Energy* **2023**, *48*, 10941–10954; d) S. I. Hossain, M. A. Aziz, S. Shanmugam, *ACS Sustain. Chem. Eng.* **2020**, *8*, 1998–2007.
[12] a) M. Pahlevaninezhad, E. E. Miller, L. Yang, L. S. Prophet, A. Singh, T. Storwick, M. Pahlevani, M. A. Pope, E. P. L. Roberts, *ACS Appl. Energy Mater.* **2023**, *6*, 6505–6517; b) X. Meng, Q. Peng, J. Wen, K. Song, L. Peng, T. Wu, C. Cong, H. Ye, Q. Zhou, *J. Appl. Polym. Sci.* **2023**, *140*, e53802.
[13] a) J. Lu, A. Barnett, V. Molinero, *J. Phys. Chem. C* **2019**, *123*, 8717–8726; b) K. Oh, M. Moazzam, G. Gwak, H. Ju, *Electrochim. Acta* **2019**, *297*, 101–111.
[14] a) M. Rezayani, F. Sharif, H. Makki, *J. Phys. Chem. C* **2023**, *127*, 8462–8472; b) P. Sharma, V. K. Shahi, *ACS Appl. Mater. Interfaces* **2023**, *15*, 9171–9181; c) B. Ameduri, DOI: 10.1002/0471440264.pst137.pub2, Wiley **2023**; d) B. Ameduri, B. Boutevin, *J. Fluorine Chem.* **2005**, *126*, 221–229.
[15] a) A. K. Nandi, R. Ghosh, D. P. Chatterjee, *Reactive and Functional Polymers Volume Two: Modification Reactions, Compatibility and Blends* (Ed: T. J. Gutiérrez), Springer International Publishing, Cham **2020**, pp. 283–324, DOI: 10.1007/978-3-030-45135-6 10; b) H. Zhang, C. Mingxue, H. Xin, F. Liang, L. Chunhua, H. Tingting, *Progr. Chem.* **2021**, *33*, 596–609; c) G. Zapsas, Y. Patil, Y. Gnanou, B. Ameduri, N. Hadjichristidis, *Progr. Polym. Sci.* **2020**, *104*, 101231.

[16] J. Cao, Z. Yuan, X. Li, W. Xu, H. Zhang, *J. Power Sources* **2015**, *298*, 228–235.
[17] S. Yoon, E. Lee, S. J. Yoon, D. M. Yu, Y. J. Kim, Y. T. Hong, S. So, *ACS Appl. Energy Mater.* **2021**, *4*, 4473–4481.
[18] L. Ling, M. Xiao, D. Han, S. Ren, S. Wang, Y. Meng, *J. Membr. Sci.* **2019**, *585*, 230–237.
[19] X. Yang, H. Zhu, F. Jiang, X. Zhou, *J. Power Sources* **2020**, *473*, 228586.
[20] U. Dalal, M. Kapoor, A. Verma, *Energy Fuels* **2023**, *37*, 13457–13466.
[21] S. Sreenath, P. S. Nayanthara, C. M. Pawar, D. Y. Nikumbe, B. Bhatt, J. C. Chaudhari, R. K. Nagarale, *ACS Appl. Energy Mater.* **2022**, *5*, 13661–13671.
[22] L. Hu, L. Gao, M. Di, X. Yan, X. Jiang, X. Wu, G. He, X. Li, *J. Mater. Chem. A* **2022**, *10*, 3430–3435.
[23] P. P. Sharma, V. Yadav, S. Gahlot, O. V. Lebedeva, A. N. Chesnokova, D. N. Srivastava, T. V. Raskulova, V. Kulshrestha, *J. Membr. Sci.* **2019**, *573*, 485–492.
[24] A. Rajput, H. Khan, S. K. Raj, R. Kothandaraman, V. Kulshrestha, *Mater. Adv.* **2020**, *1*, 1930–1938.
[25] J. Sharma, C. Totee, V. Kulshrestha, B. Ameduri, *Eur. Polym. J.* **2023**, DOI: 10.1016/j.eurpolymj.2023.112580112580.
[26] J. Sharma, R. Gupta, S. Mishra, K. Ramanujam, V. Kulshrestha, *ACS Appl. Mater. Interfaces* **2023**, *15*, 44899–44911.
[27] H. Chen, G. R. Palmese, Y. A. Elabd, *Chem. Mater.* **2006**, *18*, 4875–4881.
[28] X. Zhang, T. Liu, S. Zhang, X. Huang, B. Xu, Y. Lin, B. Xu, L. Li, C.-W. Nan, Y. Shen, *J. Am. Chem. Soc.* **2017**, *139*, 13779–13785.
[29] a) M. Guerre, M. Semsarilar, C. Totée, G. Silly, B. Améduri, V. Ladmiral, *Polym. Chem.* **2017**, *8*, 5203–5211; b) P. Kaner, A. V. Dudchenko, M. S. Mauter, A. Asatekin, *J. Mater. Chem. A* **2019**, *7*, 4829–4846.
[30] Y.-C. Chiang, Y. Chang, A. Higuchi, W.-Y. Chen, R.-C. Ruaan, *J. Membr. Sci.* **2009**, *339*, 151–159.
[31] S. Mishra, J. Sharma, N. H. Rathod, V. Kulshrestha, *ACS Appl. Energy Mater.* **2022**, *5*, 4850–4860.
[32] Y. Zhu, L. Ding, X. Liang, M. A. Shehzad, L. Wang, X. Ge, Y. He, L. Wu, J. R. Varcoe, T. Xu, *Energy Environ. Sci.* **2018**, *11*, 3472–3479.
[33] P. Patnaik, S. M. Hossain, S. Pal, S. Sarkar, R. Sharma, U. Chatterjee, *J. Membr. Sci.* **2023**, *688*, 122105.
[34] D. C. Herbst, T. A. Witten, T.-H. Tsai, E. B. Coughlin, A. M. Maes, A. M. Herring, *J. Chem. Phys.* **2015**, *142*.
[35] Y. Zheng, U. Ash, R. P. Pandey, A. G. Ozioko, J. Ponce-González, M. Handl, T. Weissbach, J. R. Varcoe, S. Holdcroft, M. W. Liberatore, R. Hiesgen, D. R. Dekel, *Macromolecules* **2018**, *51*, 3264–3278.
[36] a) M. A. Izquierdo-Gil, V. M. Barragán, J. P. G. Villaluenga, M. P. Godino, *Chem. Eng. Sci.* **2012**, *72*, 1–9; b) R. S. Kingsbury, K. Bruning, S. Zhu, S. Flotron, C. T. Miller, O. Coronell, *Ind. Eng. Chem. Res.* **2019**, *58*, 18663–18674; c) E. Sireci, G. De Luca, J. Luque Di Salvo, A. Cipollina, G. Micale, *J. Membr. Sci.* **2023**, *668*, 121283.
[37] a) J. S. Lawton, A. M. Jones, Z. Tang, M. Lindsey, C. Fujimoto, T. A. Zawodzinski, *J. Electrochem. Soc.* **2016**, *163*, A5229; b) R. A. Elgammal, Z. Tang, C.-N. Sun, J. Lawton, T. A. Zawodzinski, *Electrochim. Acta* **2017**, *237*, 1–11.
[38] a) A. Almomani, L. Granadillo, W. Hong, R. Montazami, *Mater. Res. Express* **2018**, *5*, 065325; b) T. Okada, Y. Ayato, M. Yuasa, I. Sekine, *J. Phys. Chem. B* **1999**, *103*, 3315–3322; c) T. Luo, F. Roghmans, M. Wessling, *J. Membr. Sci.* **2020**, *597*, 117645; d) A. Münchinger, K.-D. Kreuer, *J. Membr. Sci.* **2019**, *592*, 117372.
[39] a) S. Zhu, R. S. Kingsbury, D. F. Call, O. Coronell, *J. Membr. Sci.* **2018**, *554*, 39–47; b) J. Sharma, S. K. Misra, V. Kulshrestha, *Chem. Eng. J.* **2021**, *414*, 128776.
[40] a) K. W. Han, K. H. Ko, K. Abu-Hakmeh, C. Bae, Y. J. Sohn, S. S. Jang, *J. Phys. Chem. C* **2014**, *118*, 12577–12587; b) K.-D. Kreuer, *Chem. Mater.* **1996**, *8*, 610–641.
[41] a) R. Fang, H. Zhang, L. Yang, H. Wang, Y. Tian, X. Zhang, L. Jiang, *J. Am. Chem. Soc.* **2016**, *138*, 16372–16379; b) C. Zhao, J. Hou, M. Hill, B. Freeman, H. Wang, H. Zhang, *Acc. Mater. Res.* **2023**, *4*, 786–797.
[42] a) E. Schönemann, A. Laschewsky, A. Rosenhahn, *Polymers* **2018**, *10*; b) W. Zhao, P. Fonsny, P. FitzGerald, G. G. Warr, S. Perrier, *Polym. Chem.* **2013**, *4*, 2140–2150.
[43] B. Ameduri, *Prog. Polym. Sci.* **2022**, *133*, 101591.

Manuscript received: September 18, 2024
Revised manuscript received: October 9, 2024
Version of record online: ■■, ■■

RESEARCH ARTICLE

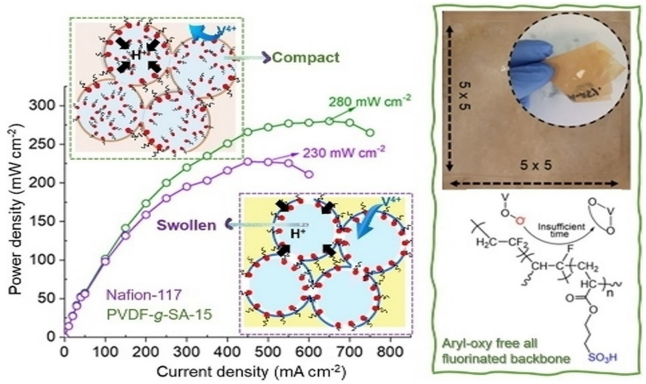

A protogenic membrane bearing halato-telechelic $-SO_3H$ architecture for efficient vanadium redox flow batteries is developed. The designed fluorinated membrane achieves efficient proton conductivities, vanadium barricading properties and high oxidative stabilities desired for terrestrial applicability. Optimized membrane exhibits superior performance, operates with 98% capacity utilization, delivers ~7 Watt power densities at bench-scale and holds promising utility in VRFB applications.

J. Sharma, B. Améduri, V. Kulshrestha**